

Numerical and Experimental Investigation of Slanted Axial-flow pumping System

Fan Yang* and Chao Liu

¹College of water resources and Energy power Engineering, Yangzhou University, Yangzhou - Jiangsu - China

²Hydrodynamic Engineering Laboratory of Jiangsu Province, Yangzhou-Jiangsu- China

Received 29 June 2013; Accepted 25 July 2013

Abstract

The Investigation of the three-dimensional (3D) fluid flow inside a slanted axial pumping system, based on the Reynolds time-averaged Navier-Stokes equations and the RNG $k-\epsilon$ turbulent flow model, applying the multiple reference frames. The flow detail of whole slanted axial pumping system is attained. The relation between hydraulic performance of outlet sections with rotating impeller and installation height of pumping system and the stress distribution of impeller is analyzed, so is the relative velocity distribution near the airfoil cross sections under the designed condition. The hydraulic moment under different conditions was calculated based on the numerical results, and the changing features of hydraulic moment on blades with flow rates are analyzed. The reference nominal height of pump is put forward. The comparison of simulation results and the experiment data shows that the calculation performance closes agrees with the experiment results at the best efficiency and designed operating conditions, but under the condition of low rate, deviations exist between the two results. Using CFD method to simulate the internal flow field of slanted axial pumping system can provide the basis for the hydraulic design of the slanted axial pumping system or its optimization.

Keywords: Pumping system, Impeller, Hydraulic moment, Hydraulic performance, Numerical investigation, Model test

1. Introduction

According to the angle between the axis of the pump and horizontal line, pumping system can be classified as three basic types: vertical pumping system, horizontal pumping system and slanted pumping system. The slanted pumping system has the advantages of vertical and horizontal pumping system, the net lift of which lies between others. Slanted pumping system has the following properties: simpler but more compact structure, less excavation volume, lower pump house, pump house bottom board uniformly forced and so on. For the slanted pumping system operating longer time yearly, the reliability of water pilot bearings is queried, so that this structure type has not been widely used in china, furthermore, the application of slanted pumping system is tabled in south-to-north water transfer east route project. The slanted pumping system has been used for several decades in foreign countries, while in China only about 20 years. China's first slanted pumping system built in 1991 to run for the Red Gebo station in Inner Mongolia, subsequently, China developed its own slanted pumping system which was used in Tie ShanZui of Hunan province and Xing-XiaGang of Jiangsu province. In addition, YanGuan pumping system of Taihu Lake watershed management project in Zhejiang province and Taihu river pumping system in Shanghai also used the kind type of

slanted pump devices [1].

Wang used CFD model to analyze the impeller elevation, unsteady flow, hydraulic thrust and the zero-head flow characteristics of the pump [2]. Peng used Fluent soft to simulate steady and unsteady flows in a large slanted axial pump at the Taihu River pumping station for near-zero head conditions [3]. Lu calculated the flow field in various passages with oblique pumping system with finite element method [4]. The correlative reports of foreign research are few. Currently, the research on the slanted pumping system is insufficient at home and abroad, so it is necessary to study the slanted pumping system, which can further enrich the application type of low-lift pumping system. The flow field in the pumping system was simulated and measured in many studies in recent years [5-12]. Based on the RANS equations and RNG turbulence model, the three-dimensional flow field in slanted pumping system was simulated by CFD, the interior and external characteristic of pumping system was analyzed. For verifying the accuracy and reliability of the calculation results, a model test was conducted.

2. Numerical models

2.1 Governing equations

The governing equations for the turbulent incompressible flow encountered in this research are the Reynolds-Averaged Navier-Stokes equations for the conservation of mass and momentum, given as [13]:

* E-mail address: sqzyangfan@126.com

$$\frac{\partial \rho}{\partial t} + \frac{\partial}{\partial x_i} (\rho \bar{u}_i) = 0 \quad (1)$$

$$\frac{\partial}{\partial x_i} (\rho \bar{u}_i \bar{u}_j) = -\frac{\partial \bar{p}}{\partial x_i} + \frac{\partial}{\partial x_j} \left(\mu \frac{\partial \bar{u}_i}{\partial x_j} - \rho \overline{u'_i u'_j} \right) + S_i \quad (2)$$

To correctly account for turbulence, the Reynolds stresses are modeled in order to achieve the closure of Eq.2. The modeling is based on the Boussinesq hypothesis to relate the Reynolds stress to the mean velocity gradients within the flow. The Reynolds stresses are given by

$$-\rho \overline{u'_i u'_j} = \mu_t \left(\frac{\partial \bar{u}_i}{\partial x_j} + \frac{\partial \bar{u}_j}{\partial x_i} \right) - \frac{2}{3} \delta_{ij} \cdot \left(\rho k + \mu_t \frac{\partial \bar{u}_i}{\partial x_i} \right) \quad (3)$$

For two-equation turbulence models, such as the $k-\varepsilon$ variants, the turbulent viscosity is computed through the solution of two additional transport equations for the turbulent kinetic energy k , and the turbulence dissipation rate ε .

2.2 Turbulence model

The turbulence effects were modeled by the RNG $k-\varepsilon$ two-equation turbulence model, which provides an option to account for the effects of swirl or rotation by modifying the turbulent viscosity appropriately. A more comprehensive description of RNG theory and its applications to turbulence computation can be found in Ref. [13]. The RNG $k-\varepsilon$ two-equation turbulence model is expressed for turbulent kinetic energy k and viscous dissipation ε respectively as follows:

$$\frac{\partial(\rho k)}{\partial t} + \frac{\partial(\rho \bar{u}_j k)}{\partial x_j} = \frac{\partial}{\partial x_j} \left(\Gamma_k \frac{\partial k}{\partial x_j} \right) + p_k - \rho \varepsilon \quad (4)$$

$$\frac{\partial(\rho \varepsilon)}{\partial t} + \frac{\partial(\rho \bar{u}_j \varepsilon)}{\partial x_j} = \frac{\partial}{\partial x_j} \left(\Gamma_\varepsilon \frac{\partial \varepsilon}{\partial x_j} \right)$$

$$+ \frac{\varepsilon}{k} (C_{\varepsilon 1} p_k - \rho C_{\varepsilon 2} \varepsilon) \quad (5)$$

Where

$$\Gamma_k = \mu + \frac{\mu_t}{\sigma_k}; \quad \Gamma_\varepsilon = \mu + \frac{\mu_t}{\sigma_\varepsilon}$$

$$p_k = \mu_t \left(\frac{\partial \bar{u}_i}{\partial x_j} + \frac{\partial \bar{u}_j}{\partial x_i} \right) \cdot \frac{\partial \bar{u}_i}{\partial x_j};$$

$$C_{1\varepsilon} = 1.44 - \frac{\eta \left(1 - \frac{\eta}{\eta_0} \right)}{\left(1 + \beta \eta^3 \right)}; \quad \eta = S \frac{k}{\varepsilon}$$

$$S = \sqrt{\left(\frac{\partial \bar{u}_i}{\partial x_j} + \frac{\partial \bar{u}_j}{\partial x_i} \right) \cdot \frac{\partial \bar{u}_i}{\partial x_j}}$$

$$C_\mu = 0.0845; C_{\varepsilon 1} = 1.42; C_{\varepsilon 2} = 1.68; \sigma_k = 1.39$$

$$\sigma_\varepsilon = 1.39; \eta_0 = 4.377; \beta = 0.012.$$

2.3 Computational parameters and boundary conditions

The 15° slanted axial-flow pump operating at 1498.3r/min rotational speed is chosen as sample for experiment. The diameter of the 3-bladed impeller is 300mm. The tip clearance of impeller is 0.2mm at blade angle 0°, which are the same as those of the experiment model. The computational domain consists of slanted elbow inlet passage, the impeller with three blades, the diffuser with eight vanes and slanted outlet passage. The corresponding three-dimensional model is shown in Fig.1.

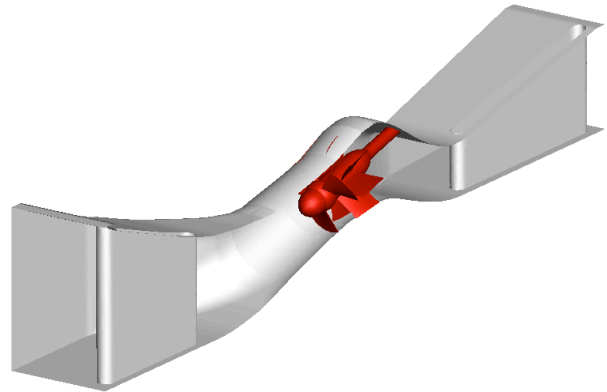
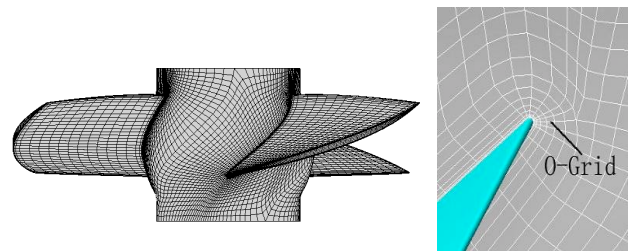


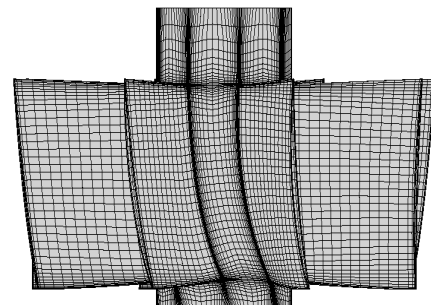
Fig. 1. Perspective of slanted axial-flow pumping system

2.4 Grid generation

The geometry of pumping system is complex which including inlet passage, impeller, guide vane and outlet passage. A structured grid system was constructed in the impeller and guide vane, which has O-type grids around the blade surfaces and H/J-type grids in other regions. All of them are composed of hexahedral grid system as shown in Fig.2. The tetrahedral unstructured grid cell was used in inlet and outlet passage to generate the mesh.



(a) Impeller



(b) Guide vane

Fig.2 Computational grids of impeller and guide vane

3. Results and discussion

3.1 Flow field of pumping system

The flow field of pumping system is shown in Fig.3 at the best efficiency condition ($K_Q=0.518$). In the oblique line segment region of elbow-shaped and slanted inlet passage, the internal flow pattern is uniform, smooth, and gradually velocity increases, then flow begin to turn, and run into the elbow-shaped and slanted region, so that the inboard velocity is higher than outboard velocity. The distribution of velocity is relative uniform, because turning angle of elbow bend is small. Given that the impeller is rotating, guide vane is recycling the pressure energy and controlling the circulation, when the water flow merges into outlet passage from all around, because of the constraints and the effects of the outlet passage wall, with uneven velocity, especially, for the part inside the pier, the water flowing from top to bottom, and that from bottom to top, merge into a whirling shape flow, and it is easy to produce flow separation and vortex, increasing hydraulic loss, thus it plays an important role in the hydraulic performance of pumping system.

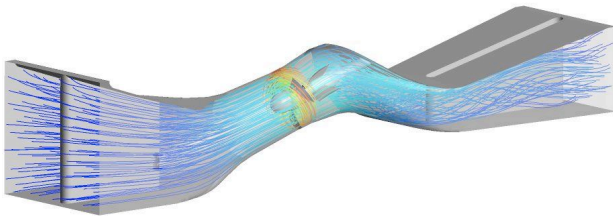


Fig. 3 Internal particle path of slanted axial-flow pumping system

In order to investigate the hydraulic performance of inlet passage and outlet passage, the variable law of hydraulic loss was analyzed by using the hydraulic loss coefficient K . The hydraulic loss coefficient K was defined as follows:

$$K = \frac{\Delta h}{H} \times 100\% \quad (6)$$

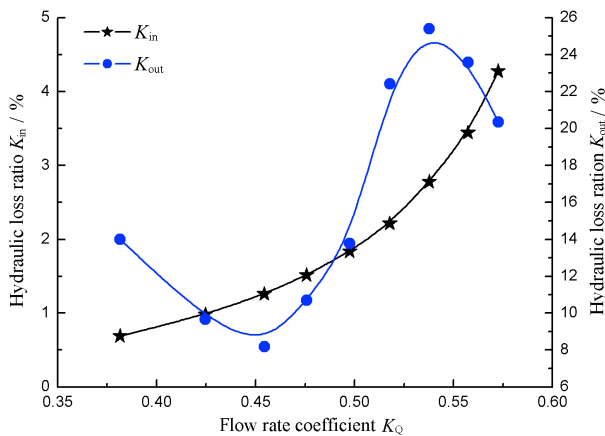


Fig. 4 Hydraulic loss ratio and flow rate coefficient

Fig.4 shows the hydraulic loss of inlet passage increases gradually with the increase of flow rate, while that of outlet passage doesn't appear regular change. The hydraulic loss of outlet passage consists of the frictional head loss, local head loss and circulation loss, on which outlet circulation of the guide vane has great influence. At the designed condition,

circulation loss is small, but at other conditions, circulation loss can increase, even exceed the sum of frictional head loss and local head loss, the hydraulic loss of outlet passage is relatively large at non high efficiency area. This is also the main reason to explain the different of hydraulic loss of outlet passage and that of inlet passage. The hydraulic loss of outlet passage accounts for more percentage, and has great influence on the performance of pumping system. Type line of outlet passage is optimized, which is an important breakthrough to improve performance of pumping system.

3.2 Flow distributing law of outlet sections

The slanted 15° inlet passage is composed of line segment and curved segment. The main control size of the slanted 15° inlet passage includes the inlet height of impeller H_{in} , the length of the horizontal projection L , the diameter of impeller D , the upper contraction angle α and the nominal height of impeller H_w . The schematic diagram of inlet passage is shown in Fig.5.

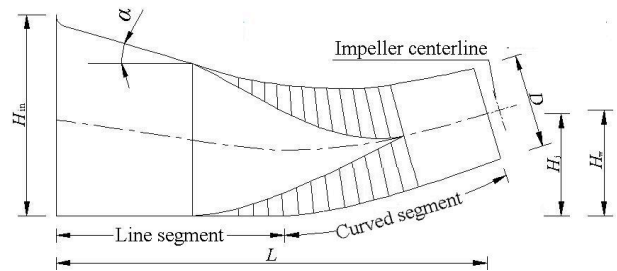


Fig. 5 Schematic diagram of inlet passage

The relative height of cross section H_n is calculated by

$$H_n = \frac{H_i}{D} \quad (7)$$

Where H_j is the height of cross section from the bottom of inlet passage.

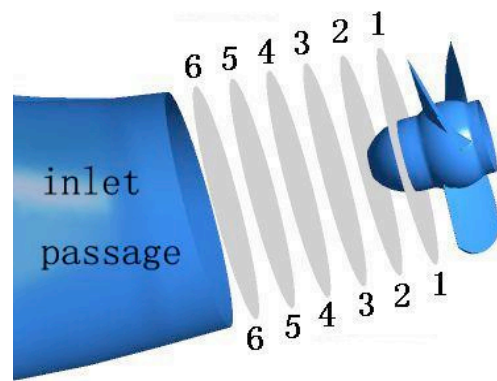


Fig. 6 Cross sections

The position of cross sections is shown in Fig.6, For each section, the relative height of cross section H_n is sequence of 1.02、1.00、0.95、0.90、0.85 and 0.80. Further study on hydraulic performance of each section at the outlet of inlet passage, the mathematical model of hydraulic performance was established by taking the velocity-weighted average swirl angle θ and the axial

velocity distribution uniformity V_{z+} as objective function. The axial velocity distribution uniformity and the velocity-weighted average swirl angle were defined as follows:

$$V_{z+} = \left\{ 1 - \frac{1}{\bar{v}_a} \sqrt{\sum_{i=1}^m (v_{ai} - \bar{v}_a)^2 / n} \right\} \times 100\% \quad (8)$$

$$\theta = \frac{\sum_{i=1}^m v_{ai} \left[90^\circ - \arctan \frac{v_{ti}}{v_{ai}} \right]}{\sum_{i=1}^m v_{ai}}$$

Where \bar{v}_a , v_{ai} , v_{ti} indicate the weighted arithmetic mean of axial velocity, the axial velocity of every calculation unit, the transverse velocity of every calculation unit.

Calculation results of design condition ($K_Q=0.498$) are shown in Fig.7. The velocity-weighted average swirl angle and the axial velocity distribution uniformity is lower in outlet section 1-1, because it is affected by impeller rotating, while the value of hydraulic performance don't necessarily mean better, with the decrease of the position between cross section and impeller. Optimal cross section is obtained by separate numerical simulation of inlet passage without impeller, while it is affected by impeller rotating in the whole flow passage of the pumping system, so that axial velocity aren't perpendicular to inlet section of impeller.

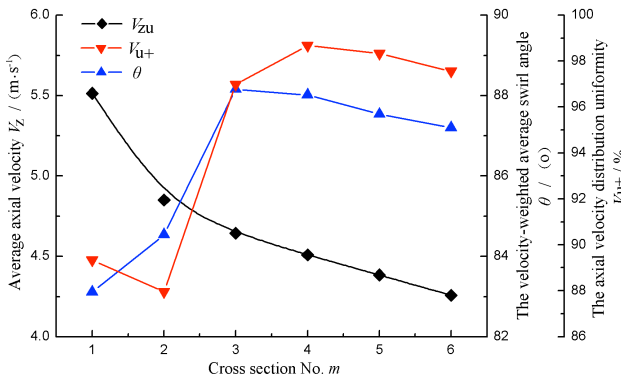


Fig. 7 The hydraulic performance of cross sections

Calculation results of design condition ($K_Q=0.498$) are shown in Fig.7. The velocity-weighted average swirl angle and the axial velocity distribution uniformity is lower in outlet section 1-1, because it is affected by impeller rotating, while the value of hydraulic performance don't necessarily mean better, with the decrease of the position between cross section and impeller. Optimal cross section is obtained by separate numerical simulation of inlet passage without impeller, while it is affected by impeller rotating in the whole flow passage of the pumping system, so that axial velocity aren't perpendicular to inlet section of impeller.

The nominal height of H_w was defined as follows:

$$H_w = \frac{H_Y}{D} = \frac{H_Y}{D} + \frac{L_Y \sin 15^\circ}{2D} \quad (9)$$

Where H_Y is the height of impeller centerline from bottom of inlet passage, L_Y is the length of impeller chamber along the flow direction.

The nominal height range of impeller in the elbow-shaped and slanted inlet passage can be marked from $(0.7\sim 0.9)D$ by calculation and experiment, so as to sure the value of the axial velocity distribution uniformity and the velocity-weighted average swirl angle can be better, and the low height characteristics of the passage can be proved.

3.3 Hydraulic performance of impeller

Rotating impeller is subjected to water pressure, centrifugal force, mechanical friction and otherwise. Because Rotating speed is constant, centrifugal force is also constant, and mechanical friction is inevitable, only managing to decrease. With the change of operating condition, the stress characteristics of blade change under the action of flow. Flow force contours are shown in Fig.8, in 3 different operating conditions. With the increase of flow rate, force of blade surface decrease gradually. Under different cases, maximum force lies in the leading side of pressure surface, while minimum force lies in the leading side of suction surface, and flow force of pressure surface increase gradually from hub to shroud. There is a slight difference between flow forces of three blades, mainly because the distribution of velocity is uneven in inlet section. The force difference of 3 blades leads to impeller vibrating. With the change of force, pump characteristic curve changes, so that working head is different from theoretical head.

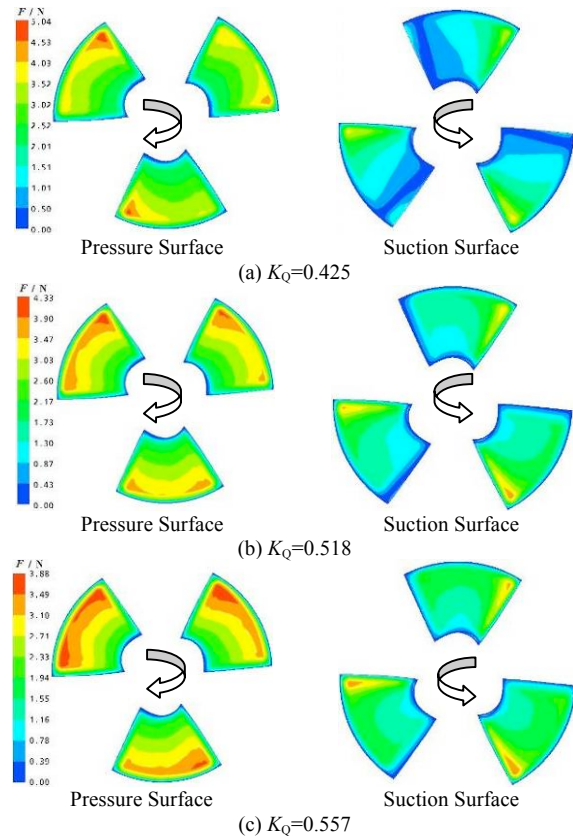


Fig. 8 Flow force distribution of blades in different operating conditions

Study on hydraulic moment which is an important mechanical property of impeller, in order to provide reference for pump regulating mechanism. The hydraulic moments under different conditions were calculated based on the computed results. Pressure is defined as follows:

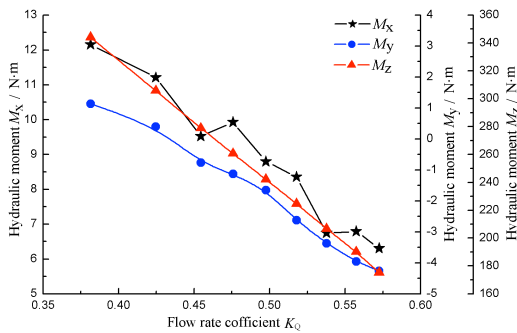
$$P = f(x, y, z) \quad (10)$$

Where x, y, z indicate coordinate value of every computational node.

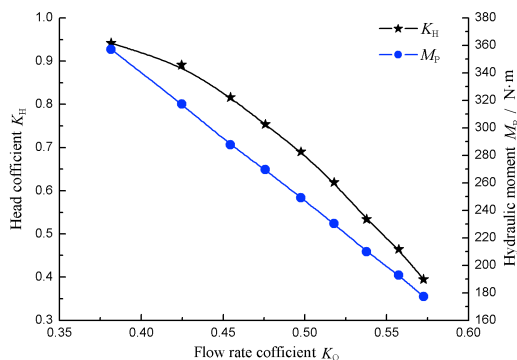
The coordinate value of any point in blade surface is (x_i, y_i, z_i) , total pressure is $P_i(x_i, y_i, z_i)$, the projection value of three coordinate orientations is respectively P_{xi}, P_{yi}, P_{zi} in rectangular coordinate system. The direction of total pressure is the same as that of normal T_{Ai} in this computational node of blade surface, which points perpendicularly to the blade surface. Then, 3D coordinate data of any two points in petiole of blade is (x_1, y_1, z_1) and (x_2, y_2, z_2) . According to theoretical mechanics, the product of pressure $P_i(x_1, y_1, z_1)$ and arm of force e_i is defined as dM_{hi} , so that the sum of hydraulic moment for all nodes is defined as:

$$M_h = \sum_{i=1}^m dM_{hi} \quad (11)$$

The computational results is shown in Fig.9, based on calculation and analysis of hydraulic moment under 9 operating conditions at the same rotating speed, and Z axis is Axial direction, X axis is transverse direction and Y axis is longitudinal direction, M_x, M_y and M_z is respectively hydraulic moment in each direction, M_p is the sum of hydraulic moment in each direction. With the increase of flow rate, M_y, M_z and M_p decrease, the overall trend of them is the same as that of head, while M_x changes constantly. The conclusions obtained by CFD are the same as that by experiment in literature [14]. The change of hydraulic moment on blades is closely related with pump characteristics, which should arouse the attention of pump designers.



(a) Hydraulic moment and flow rate



(b) Hydraulic moment, head and flow rate

Fig. 9 Calculation results of hydraulic moment

The relative velocity distribution near airfoil cross-sections under designed condition is analyzed, and the vector diagram is shown in Fig.10. With the change of the Span position, airfoil changes constantly. In Span=0.05, flow separation appears in the tail of airfoil, shown in Fig.10a-2, in others, flow separation and vortex aren't appeared.

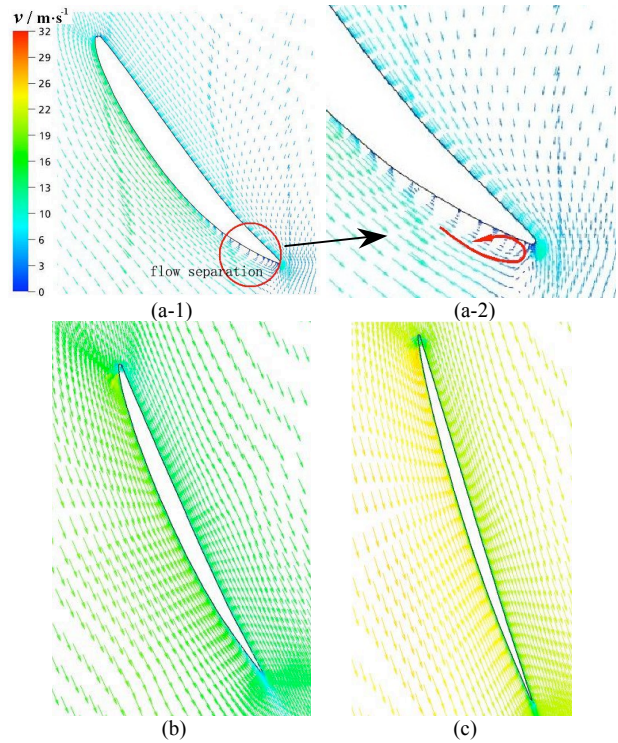


Fig. 10 Vector diagram of flow around Airfoil (a-1) Span=0.05 (b) Span=0.50 (c) Span=0.95

3.4 Pumping system performance

For the performance presentations, the flow coefficient K_Q , the head coefficient K_H , and efficiency η were defined as follows:

$$K_Q = \frac{Q}{nD^3}; K_H = \frac{gH}{n^2 D^2}; \eta = \frac{\rho g Q H}{T_p \omega}$$

Where T_p is torque of impeller.

Table 1: Optimum hydraulic performance parameters of pumping system at five blade angles

Angle $\Phi / (^\circ)$	Flow rate coefficient K_Q	Head coefficient K_H	Efficiency $\eta / \%$	Specific speed n_s
+6	0.625	0.265	72.52	1194
+4	0.592	0.246	73.96	1228
+2	0.569	0.224	75.23	1290
0	0.518	0.227	75.80	1221
-2	0.481	0.216	76.13	1222

The purpose of model test is to verify the simulation results for credibility of the numerical simulation results. The pumping system was manufactured according to the 3D model, and tested over the operational rang at five blade angles (+6°, +4°, +2°, 0°, -2°). The pumping system model

is shown in Fig.11. The overall performance curves of the model pumping system with rotor diameter $D=300\text{mm}$ and the rotation speed $n=1498.3\text{ r/min}$ are shown in Fig.12 and optimal efficiency points at five blade angles can be seen in Table.1. The efficiency at blade angle $\Phi = -2^\circ$ reaches 76.13%, which is the better efficiency in china.

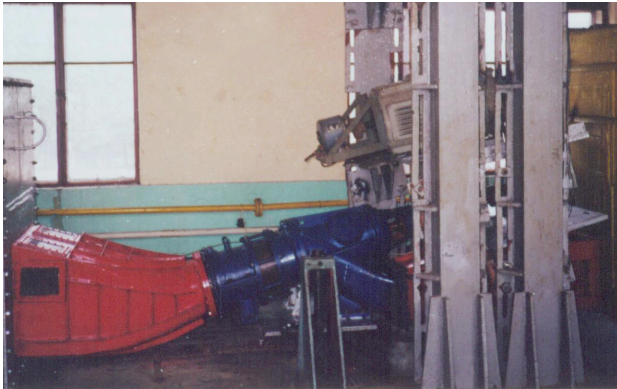


Fig. 11 Photography of pumping system model

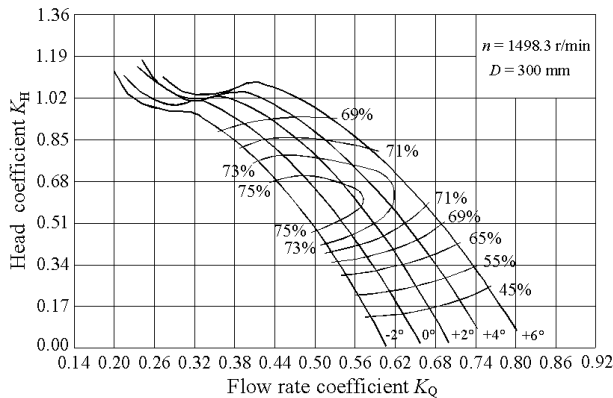


Fig. 12 Overall performance curves of pumping system

The performance of the pump as predicted from the CFD model is compared to the experimental results. As is shown in Fig.13, it proved a close agreement between predicted and experimental head coefficients, with exception of the lower flow coefficients, where it is actually over-predicted. While the deviation of the efficiency between calculated and measured results does exist in non high efficiency area. The difference between the simulation and experiment may be caused by the facts that the mechanical losses exists in the test system are not being modeled in the simulations, and the unsteady feature of flow between impeller and guide vane is not considered. The computational results are still unable to predict accurately the pumping system performance outside the high efficiency area, which need to be further improved.

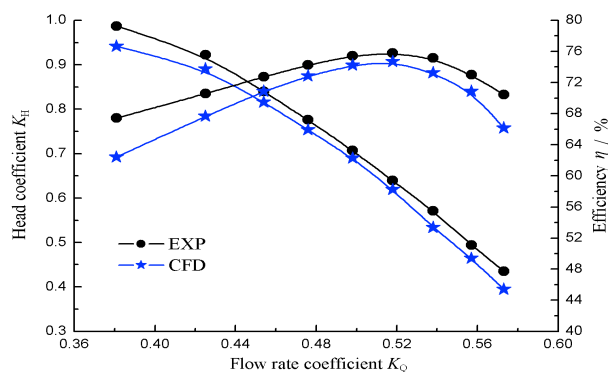


Fig. 13 Experimental and predicted results

4. Conclusions

Numerical simulation is made for a slanted pumping system. Both the internal flow fields and the external performance of the system are calculated and predicted. The relation between the axial flow distributing law of inlet passage with rotating impeller and installation height of pumping system, and the hydraulic performance of impeller are analyzed.

Comparing the calculated results with the experimental date, a good agreement was found for high efficiency area between calculated and measured results, which can meet the requirement of practical application.

Three-dimensional contraction deformation of elbow-shaped and 15° slanted inlet passage is very small, and turning angle of flow direction is also small, so that flow is steady, hydraulic loss is small relatively. The nominal height range of impeller in the elbow-shaped and slanted inlet passage can be marked from $(0.7\sim 0.9) D$ by calculation, so as to sure the value of the axial velocity distribution uniformity and the velocity-weighted average swirl angle can be better. The velocity distribution of outlet section is correlated with blade number. Slanted outlet passage has great influence on the performance of pumping system. Type line of outlet passage is optimized, which is an important breakthrough to improve performance of pumping system.

With the increase of flow rate, force of blade surface decrease gradually. Under different cases, maximum force lies in the leading side of pressure surface, while minimum force lies in the leading side of suction surface, and flow force of pressure surface increase gradually from hub to tip.

The accuracy of numerical simulation is needed to prove by the model test, and the model test can provide boundary conditions for the numerical simulation, but is the best method is modern flow testing technology for studying internal flow field in pumping system, for example: LDV (Laser Doppler Velocimetry) , PIV (Particle Imaging Velocimetry) and so on. A characteristic of slanted pumping system is high noise, how to analyze noise is worth further studying based on the numerical results. All these remains to be further elucidated.

Nomenclature

\bar{p}	Averaged pressure (Pa)
$-\rho \overline{u_i u_j'}$	Reynolds stress
k	Turbulent kinetic energy
Δh	Hydraulic loss
H	The net lift of pumping system
K	Hydraulic loss coefficient
M	Hydraulic moment
D	Impeller diameter (m)
m	Number of calculation unit
n	Rotating speed
Q	Volume flow rate

Greek letters

μ	Molecular viscosity (kg/m s)
g	Acceleration of gravity (m/s^2)
ρ	Density (kg/m^3)
ω	Angular speed (rad/s)

Subscripts

t	Turbulent
in	Inlet passage

outlet Outlet passage

This project is supported by National Science Foundation of China(Grant No.51279173), JiangSu Province colleges of Natural Science Major Project(Grant No.11KJA570001).

Acknowledgment

Support for construction/assembly of the facility was also provided by JSS Key Lab of Hydrodynamic Engineering.

References

1. Liu, C., "Pump and Pumping station", China water conservancy and hydropower Press, 174, 2009.
2. Wang, Z.W., Peng,G.J., Zhou, L.j. and Hu, D.Y., "Hydraulic performance of a large slanted axial-flow pump", Engineering Computations, 27(2): 243-256, 2010.
3. Peng, G.J., Wang, Z.W., Luo, Y.Y. and Yan, Z.G., "Journal of Tsinghua University(Sci & Tech)", 47(11): 2006-2009, 2007.
4. Lu, L. G. and Feng, H.M., "Optimum design for the inlet passage with oblique pump set", Journal of Agricultural College, 11(3): 61-67, 1990.
5. KIM Jin-Hyuk, AHN Hyung-Jin. and KIM Kwang-Yong., "High-efficiency design of a mixed-flow pump", Science China, 53(1): 24-27, 2010.
6. Yuan, S.Q., Ni, Y.Y., Pan Z.Y. and Yuan, J.P., "Unsteady turbulent simulation and pressure fluctuation analysis for centrifugal pumps", 22(1): 64-69, 2009.
7. Wang, F.J., Li, Y.J. and Cong, G.H., "CFD simulation of 3D flow in large-bore axial-flow pump with half-elbow suction sump", Journal of Hydrodynamic, Ser.B, 18(2): 243-247, 2006.
8. Shi, W.D, Zhang, D.S, Guan, X.F. and Leng, H.F., "Numerical and experiment investigation of high-efficiency axial-flow pump", Chinese Journal of Mechanical Engineering, 23(1): 38-44, 2010.
9. B. Jafarzadeh, A. Hajari, M.M.Alishahi, M.H. Akbari., "The flow simulation of a low-specific-speed high-speed centrifugal pump", Applied Mathematical Modelling, 35, 242-249, 2011.
10. Liu, H.L., Wang, Y., Yuan, S.Q., Tan, M.G. and Wang, K., "Effects of blade number on characteristics of centrifugal pump" , Chinese Journal of Mechanical Engineering, 23(6):742-747, 2011.
11. Yang, F., Liu, C., Tang, F.P. and Zhou, J.R., "Characteristics of flow in large vertical axial flow pumping system", Transactions of the Chinese Society for Agricultural Machinery, 40(9): 94-97, 2009.
12. Yang, F., Liu, C. and Tang, F.P., "Numerical simulation of three dimensional flow in large mixed-flow pump system", Proceedings of ASME-JSME-KSME Joint Fluids Engineering conference, July 24-29, Hamamatsu, Shizuoka, Japan, 2011.
13. Wang, F.J., "Computational fluid dynamics analysis – CFD Principles and application", Tsinghua University Press, 114-116, 2004.
14. Ni, F.S. and Liu, D.K., "Experiment and computation of hydraulic moment around blade axes of axial flow pumps", Journal of Hohai university, 16(2): 62-69, 1988.